SCIENCE CHINA
Chemistry

• COMMUNICATIONS •

September 2017 Vol.60 No.9:1180–1186
doi: 10.1007/s11426-017-9064-9

Controlled synthesis of hierarchically-structured $MnCo_2O_4$ and its potential as a high performance anode material

Zixiao Wu[1,2], Fuhai Li[1], Yonggang Sun[1,2], Deshan Bin[1,2], Junyu Piao[1,2], Xijie Lin[1,2],
Xiaochan Liu[1,2], Anmin Cao[1,2*] & Li-Jun Wan[1,2*]

[1] *CAS Key Laboratory of Molecular Nanostructure and Nanotechnology, and CAS Research/Education Center for Excellence in Molecular Sciences, Institute of Chemistry, Chinese Academy of Sciences, Beijing 100190, China*
[2] *University of Chinese Academy of Sciences, Beijing 100049, China*

Received April 7, 2017; accepted April 17, 2017; published online July 3, 2017

To satisfy the upsurging demand for energy storage in modern society, anode materials which can deliver high capacity have been intensively researched for the next generation lithium ion batteries. Typically, the binary $MnCo_2O_4$ with a characteristic coupled metal cations showed promising potential due to its high theoretical capacity and low cost. Here, by means of a well-designed synthesis control, we demonstrated a scalable process to achieve a hierarchical structure of $MnCo_2O_4$, which existed as uniform microspheres with embedded mesopores, showing favorable structural characters for high performance during a fast charge/discharge process. Our synthesis highlighted the importance of sodium salicylate as an essential additive to control the precipitation of the two involved metal cations. It was proved that a dual role was played sodium salicylate which cannot only facilitate the formation of microspheric shape, but also act as an effective precursor for the creation of inner mesopores. We confirmed that the hierarchically-structured $MnCo_2O_4$ showed outstanding performance when it was tested as an anode material in lithium ion batteries as revealed by its extraordinary cycling stability and high rate capability.

hierarchical structure, anode materials, $MnCo_2O_4$, lithium ion batteries, porous structure

Citation: Wu Z, Li F, Sun Y, Bin D, Piao J, Lin X, Liu X, Cao A, Wan LJ. Controlled synthesis of hierarchically-structured $MnCo_2O_4$ and its potential as a high performance anode material. *Sci China Chem*, 2017, 60: 1180–1186, doi: 10.1007/s11426-017-9064-9

Lithium ion batteries (LIBs) are currently widely used as power supply for portable electronics, electric vehicles and power grid applications. To satisfy the ever-increasing demand for energy storage, enormous efforts have been spent on LIBs to achieve higher energy densities and longer cycle life, which raised higher standard on the development of high performance electrode materials [1,2]. As far as anode materials are considered, the graphite-type based anode has witnessed enormous success since its invention. However, its limited capacity at 373 mA h/g make it insufficient to meet the need from future applications of energy storage systems with high energy densities [3,4]. Accordingly, battery researchers have been searching for different types of alternatives which are capable of delivering high rechargeable capacities for their potential in advanced LIBs systems. Since the pioneer work by Tarascon *et al.* [1], nanosized metal oxides became a research focus as potential anode materials due to their high capacity originated from the unique conversion reaction with lithium, which offer a bright future and promising results of nanostructures metal oxides as low cost, environmentally friendly, and safety anode materials.

Binary metal oxides, particularly $MnCo_2O_4$ with mixed transition metal cations, represent a unique category of promising anode materials with high theoretical capacity (906 mA h/g for $MnCo_2O_4$) [5]. As compared to those metal

---

*Corresponding authors (email: anmin_cao@iccas.ac.cn; wanlijun@iccas.ac.cn)

oxides with only single metal component, the spinel-structured composites leaves room further engineering in composition and structure, showing favorable characters such as high conductivity and favorable synergic effect between two different transition metals for their electrochemical reactions [5,6], resulting in increasing interest on the structural design and performance optimization of binary metal oxides for its possible application in LIBs [7–10]. For example, Guo *et al*. [11] developed a strategy to synthesize hierarchical tubular structures of Mn-based mixed metal oxides and the Mn-Co oxide electrode shows excellent specific capacitie of 1193 mA h/g at the current densities of 200 mA/g after 30 cycles.

Not surprisingly, the electrochemical performance of anode materials is highly related to their shapes and structural configurations due to the different kinetics for Li^+ transportations. Although the nanostructuring of metal oxides have succeeded in reducing the diffusion length of Li^+ to achieve a high rate capability during the fast charge/discharge process, the anode materials will be susceptible to severe side reactions due to the increased surface activity, which usually result in much aggravated irreversible capacity loss [12]. Hierarchical structures with mesopores embedded inside the microsized particles turned out to be a promising solution due to its capability to include the advantages from both the microsized aggregation and the nanosized units [13], providing a desired structural stability incorporated with mesopores to facilitate the conversion reaction of metal oxides, which are key factors for a stable output of electrochemical performance for these anode materials [14,15]. Accordingly, numerous synthesis efforts have been directed towards a controlled construction of hierarchical structure of binary metal oxides, among which the hydrothermal based routes turned out to be a very effective way [16,17]. Considering the high temperature, the complicate procedure, as well as the limited yield in the previous reports, it still remain a challenge that hierarchically-structured $MnCo_2O_4$ sample with embedded mesopores be produced through a simple and straightforward way [18,19]. Equally importantly, the synthesis should be highly scalable with reliable protocols for the structural control in different length scales towards an optimized electrochemical performance.

In our work, we reported a synthetic protocol to prepare microspheric $MnCo_2O_4$ particles with mesopores embedded inside. Such a hierarchical porous structure is achieved by using sodium salicylate (denoted as SA) as an interesting additive during the precipitation of the two metal cations of both Mn^{2+} and Co^{2+}, which was carried out in a continuous overflow reactor by using ammonia and sodium hydroxide as the precipitating agents. We confirmed that the existence of SA in the solution played a double role in the structural control. First, it can facilitate the formation of microspheric shapes of the precipitates without causing phase separation of these two different metal cations, forming uniform microspheres with organic components incorporated into the laminar structure of the secondary particles. Second, the removal of the organics in the newly-formed precursors through a heat treatment will induce mesopores into the microspheres along with the formation of the spinel phase of $MnCo_2O_4$, resulting in a hierarchical structure evidenced by a much increased specific surface area of the particles. By using this $MnCo_2O_4$ as an anode material, we confirmed that such a structural engineering assisted by SA showed promising potential for its future application in LIBs, which is revealed by the high rechargeable capacity and the extraordinary rate capability.

All reagents used in the experiment were of analytical grade without further purification. In a typical procedure, 250 mL 25% ammonia solution was added into 5 L distilled water in a home-made continuous overflow reactor. Then the solution containing mixed metal cations (0.5 M $MnSO_4$, 1 M $CoSO_4$) was pumped into the reactor through a peristaltic pump. Meanwhile, NaOH was introduced into the solution to maintain the pH at 11. 0.15 M sodium salicylate was pumped into the reaction and its flow rate was controlled to achieve a ratio of 1:10 when compared to the concentration of the total metal cations. The reaction is under vigorous stirring at 50 °C and is under the protection of argon. After reaction for 15 h, the pink precipitate was collected as the precursor for $MnCo_2O_4$, and was washed by deionized water and ethanol to remove the residual sulfate ion. The black $MnCo_2O_4$ powders were obtained by heating the pink sample at 600 °C for 2 h in air.

The powder X-ray diffraction patterns were recorded with a X-ray diffract meter (XRD, Rigaku D/max 2000, Japan) at a scanning rate of 3°/min in the 2θ range of 10°–80° with Cu K radiation (λ=1.54178 nm). The morphologies of the samples were observed by scanning electron microscopy (FESEM JSM-6700F) and a transmission electron microscope (JEM-2100F) (Hitachi, Japan). The inductively coupled plasma-atomic emission spectrometry (ICP-AES) analysis was measured on ICPE-9000 plasma atomic emission of SHIMADZU (Japan). Size contribution was analyzed by STERSIZER 3000 of Malvern (UK). The TGA was measured at a heating rate of 10 °C/min from 40 °C to 800 °C with an air flow-rate of 100 mL/min. The X-ray photoelectron spectroscopy (XPS) was performed on an ESCA LAB 220i-XL photo electronic spectrometer (Thermo VG Scientific, USA). The specific surface areas were measured following the multipoint Brunauer-Emmett-Teller (BET) procedure from the N_2 adsorption-desorption isotherms using an AUTOSORB-1-C gas sorption analyzer. The pore size distributions were determined from the adsorption branch of the isotherms by the Barrett-Joyner-Halenda (BJH) method.

The electrochemical behaviors of different samples were tested on using CR-2025-type coin cells. The electrodes were prepared by mixing the active materials, carbon black (Super-P), and binder CMC/SBR at a weight ratio of 5:3:1.5:0.5 and coating on Cu foil. The content of the active materials in each electrode is about 2 mg. The cells were assembled in an argon-filled glove boxes (O_2 and H_2O < 1 ppm) using lithium foil as the anode, a polymer separator and 1 M $LiPF_6$ in EC:EMC:DMC (1:1:1, *v*/*v*/*v*) as the electrolyte. The cells were charged and discharged galvanostatically at different current density using a battery cycler (Land Battery Test System) in the voltage range of 0.01 and 3 V at room temperature. Cyclic voltammetry (CV) and electrochemical impedance spectroscopy (EIS) were measured using an electrochemical workstation (AUTOLAB).

Briefly, Mn^{2+} and Co^{2+} co-precipitated in an alkali condition by using NaOH as the precipitant to form hydroxides of different metals. Ammonia was used as a coordinating agent, which is able to alleviate the fast precipitation process, which is easy to induce phase separation of these two metal cations. During our searching for suitable agents to control the precipitation process, we have tried different organic additives, which are expected to coordinate with these to metal cations and then facilitate their precipitation into desired shapes. The use of sodium salicylate turned out to be a favorable choice for the formation of microspheres. Figure 1(a) showed the scanning electron microscopy (SEM) image of the sample without the usage of sodium salicylate (this NaOH-precipitated precursor sample is denoted as p-MCOH). The product produced microsized particles with their diameter around 10 μm after reaction for 10 h (Figure 1(a)). A magnified SEM image in Figure 1(b) revealed that these particles were composed of plate-like subunits, forming irregular shape as a random aggregation of the nanosized objects. On the contrary, the existence of the sodium salicylate additive showed an obvious effect on the precipitation process. As shown in Figure 1, the collected sample after a same period of reaction time formed microspheric particles with a size around 14 μm (Figure 1(c)), which was obviously different from those plate-like aggregates shown in Figure 1(b) (this SA-involved precursor sample is denoted as p-SA-MCOH). A magnified SEM image (Figure 1(d)) revealed a hierarchical character of these particles in which lamellar subunits grew into microsized particles with different pores sitting in between. It is clear that sodium salicylate played an important role in the precipitation process since both the primary particles as a whole, but also the secondary ones of those plate-like subunits have turned different, forming near spherical particles with more organized surface details instead of irregular aggregates.

To have a better understanding on the role of SA, we did detailed characterizations on the collected precipitates with the focus on its crystalline structure and compositional ingredients. For a typical coprecitation process of both Mn^{2+} and Co^{2+} by NaOH, the product is identified to be the hydroxides of the mixed metals as revealed by its X-ray diffraction patterns (Figure 2(a)), which showed a typical $M(OH)_2$ with a $P\bar{3}m1$ space group ($Co(OH)_2$ JCPDS No.30-0443). It is noted that no impurity phase has been observed in the XRD curve, confirming the formation of pure $M(OH)_2$ phase with no oxidation of Mn^{2+}. Interesting, upon the addition of sodium salicylate in the reaction, the characteristic peaks of $M(OH)_2$ turned weak as observed in Figure 1(b) (Pattern B). The largely-disappeared XRD peaks of the crystalline $M(OH)_2$ revealed that the precipitation of the metal ions have been affected at the existence of sodium salicylate.

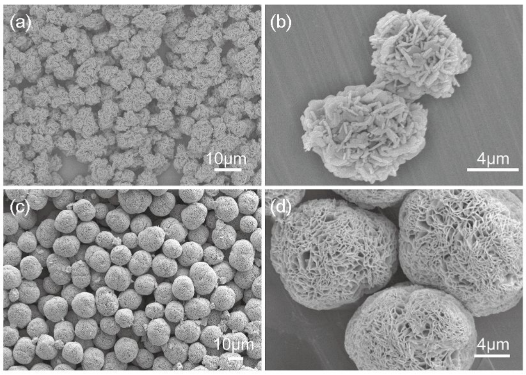

Figure 1 The SEM characterizations of the prepared samples. Low (a) and high (b) magnification SEM images of the metal hydroxide precursor prepared without the addition of SA; low (c) and high (d) magnification SEM images of the metal hydroxide precursor prepared at the existence of SA.

The elemental analysis on this p-SA-MCOH sample revealed the existence of carbon species in the precipitates assisted by sodium salicylate. As shown in Table S1 (Supporting Information online), a large amount of carbon (6.5 wt%) was detected in this precursor, disclosing the inclusion of the salicylate group during the precipitation process since the SA was the only carbon-containing species in our reaction. The Fourier transform infrared spectroscopy (FT-IR) analysis confirmed the existence of the salicylate group in the precipitate. As shown in Figure 2(b), the peaks of carboxylic (1642 cm^{-1}) and benzene skeleton (1474, 1488 cm^{-1}) in salicylate can also be found in the corresponding precipitate, verifying the inclusion of this organic groups in the collected sample. The salicylate group is known to have strong O-donor centers due to its carboxylic and hydroxyl group. Accordingly the salicylate group has been well known as a versatile ligand for the chelation of different transition metals, typically Mn^{2+} and Co^{2+}. It is expected that the precipitation of these two transition metals by NaOH have been different due to the reaction between salicylate and metal ions, forming salicylate-containing species which were able to show different morphology of precipitates with a different degree of crystallization. The elemental mapping of the particle showed an even distribution of carbon species inside with no preferential enrichment (Figure S1, Supporting Information online) in specific areas, revealing that the SA is homogeneously distributed in the particles from the

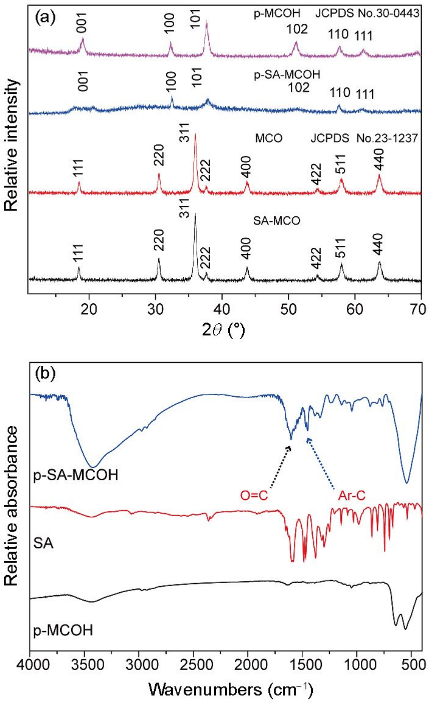

Figure 2 (a) XRD patterns of four different samples including two hydroxide precursors and two final metal oxides. The four samples are denoted as p-MCOH, p-SA-MCOH, MCO, and SA-MCO, respectively. (b) FT-IR spectra of three representative samples including p-SA-MCOH, SA, and p-MCOH, respectively. The characteristic peaks of SA could be found in the FT-IR pattern of p-SA-MCOH, confirming the existence of SA inside (color online).

precipitation process. The existence of the organic component of salicylate group can also been verified by the thermogravimetric analysis (TGA, Figure S2). The weight loss of the p-SA-MCOH during the high temperature treatment showed a much higher weight loss, which is not surprising considering the existence of the organics in the sample.

The formation of metal oxides can be achieved by heating the samples at a temperature of 600 °C for 2 h. The XRD analysis showed that both these two samples formed highly crystalline phase of $MnCo_2O_4$ (JCPDS No.23-1237, the metal oxide samples from two different precursors are denoted as MCO and SA-MCO, respectively). We have also characterized the SA-MCO sample by using the technique of d X-ray photoelectron spectroscopy (XPS) and the pattern is shown in Figure S3. The characteristic peaks of the Mn2p and Co2p curves could be readily deconvoluted to confirm the co-presentence of the solid/state redox couples of Mn^{2+}/Mn^{3+} and Co^{2+}/Co^{3+}, which agrees well with the results reported in the literatures [5,20]. A quantitative measurement has been made by inductively coupled plasma-atomic emission spectrometry (ICP-AES) to find out the ratio of Mn^{2+} and Co^{2+} in SA-MCO. The results show that in 22.5 μg/mL SA-MCO solution the concentration of Mn^{2+} and Co^{2+} are 5.15 and 11.3 μg/mL, respectively, corresponding to a Co/Mn molar ratio at 2.04, which is in good agreement with composition used in the feed stock. Our further characterization on the morphology of this sample showed that the heat treatment did not cause obvious damage on the particle shape. A measurement of particle size distributions of SA-MCO with a D50 (13.96 μm) has been made (Figure S4) to validate the conclusion. As shown in Figure 3(a), the SEM image confirmed the survival of the hierarchical structure after the high temperature treatment. A higher magnification SEM analysis in Figure S5 showed the image of the secondary particles on the surface of the micro-sized chunks, revealing a good inheritance of the hierarchical structure from its hydroxide precursor.

Inspired by the porous structure as observed in the SEM image, we have measured the N_2 adsorption-desorption isotherms of these two MCO samples (Figure 3(b)), namely the MCO and SA-MCO ones. Interestingly, we were able to observe an obvious difference between their desorption-adsorption behaviors. Hysteresis has been observed in the adsorption isotherms for the SA-MCO sample, indicating its mesoporous nature after the heat treatment, which was not observed for the MCO one. The BET test showed that the specific surface area of these two samples are 9.51 and 43.61 m^2/g (Figure S6), respectively, detailing the contribution of the newly-formed pores after the SA removal in the MCO structure. The pore size distribution has been provided (Figure S7) for a better understanding on the morphological difference between these two samples.

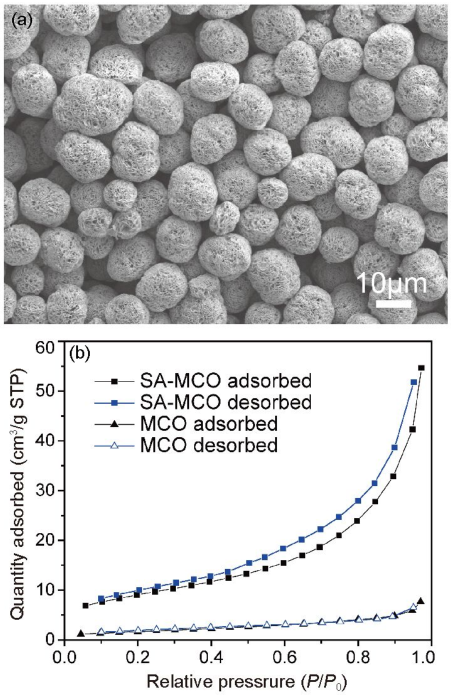

Figure 3 (a) Nitrogen adsorption-desorption isotherms of MCO and SA-MCO, respectively; (b) SEM image of the SA-MCO sample, confirming that no obvious damage has induced on the particle shape.

To have a better understanding on the inner structure of these metal oxides, we carried out systematic structural analysis with the help of transmission electron microscopy (TEM). For the MCO sample which is prepared without the assistance of SA, we found that the particle is composed of thicker layers of different subunits similar to its hydroxide precursor (Figure 4(a)). The high resolution TEM (HRTEM) characterization (Figure 4(b)) confirmed the existence of crystalline phase of $MnCo_2O_4$ as revealed by the lattice fringes, whose spacing distance was measured to be 0.252 nm. The value was in good agreement with the lattice spacing of the (311) planes. It is noted that the removal of the organics in the SA-containing precursor upon high temperature treatment would introduce a large amount of mesopores in the structures.

Figure 4(c) showed the TEM image of a randomly-picked piece of the lamella submits from the SA-MCO sample. There exist nano-sized pores all across the plate-like unit which is clearly different from the one shown in Figure 4(a). The mesopores could be clearly identified by HRTEM analysis in Figure 4(d), which showed a pore size around 10 nm embedded in the crystalline phase of MCO. Accordingly, this holey architecture of SA-MCO organized by lamellar subunits (Figure 4(b)) was endowed with more nanosized pores, showing a hierarchical structure with the existence of pores at different dimensions. It is also noted that the TEM observations on the particles are in good agreement with the data from the N_2 adsorption-desorption isotherms, confirming the critical role of SA in facilitating the formation of mesopores inside the final MCO structure.

The hierarchical structured metal oxides have showed broad potential in different application areas including energy conversion and storage devices, catalysis, and sensors [13,21,22]. The first of these potentials is investigated here by looking into the application of the prepared SA-MCO sample as an anode material in lithium ion batteries. Here we have carried detailed electrochemical characterizations by comparing the performance of the above-mentioned two MCO samples with distinct morphologies. Figure 5(a) showed the charge/discharge curves of SA-MCO sample at different cycling stages when working at a relatively-high current density of 2 A/g (around 2.208 C based on the theoretical capacity of 906 mA h/g MCO). The plateaus observed in the first cycle will have an obvious change in the following cycles along with a decrease in the discharge capacity, and leads to much smoother slopes during the continuous charge/discharge operation, showing a characteristic phenomenon probably related to the irreversible reduction reaction and the formation of the solid electrolyte interface (SEI) during the conversion of the metal oxide anode [20,23–26]. Such a change in the charge/discharge character can also be revealed by the cyclic voltammetry (CV) test as shown in Figure S8. The cathodic peak at ~1.27 V has been known to correspond to the redox couple of Co^{3+} to Co^{2+} while the sharp cathodic peak at ~0.67 V is caused by the further reduction of Co^{2+} and Mn^{2+} to metallic Co and Mn (Eq. (1)) [20,27–30]. Accordingly, there exist two oxidation peaks in the anodic scan with their positions located at ~1.53 and ~1.98 V, which are related to the oxidation of Mn to Mn^{2+} and Co to Co^{2+}, respectively (Eq. (2)) [20,27–30]. In the following cycles, the reduction peak moves to about ~0.97 V and becomes much broader, showing a typical electrochemical performance of MCO sample (Eq. (3)) which has been widely acknowledged due to the irreversible reaction and SEI formation [20,23–26]. The related reaction process can be briefly schemed below:

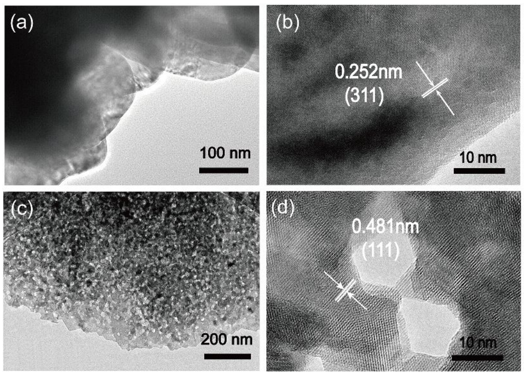

Figure 4 TEM (a, c) and HRTEM (b, d) images of two metal oxide samples. (a, b) Including MCO; (c, d) including SA-MCO.

$$MnCo_2O_4 + 8Li^+ + 8e^- = Mn + 2Co + 4Li_2O \tag{1}$$

$$Mn + 2Co + 3Li_2O = MnO + 2CoO + 6Li^+ + 6e^- \tag{2}$$

$$MnO + 2CoO + 6Li^+ + 6e^- = Mn + 2Co + 3Li_2O \tag{3}$$

It is noted that the following cycles up to 50 times exhibited a stable output as revealed by the almost identical charge/discharge curves. The discharge capacity showed in Figure 5(b) from the cyclability test confirmed a stable output of the SA-MCO anode with no noticeable capacity fading after 50 cycles. The advantage of the structural control could be clearly manifested for their battery test working at high rates. Figure 5(c) showed the batter test on the rate capability of the two samples, namely the SA-MCO and the uncontrolled sample of MCO, respectively. Typically, at a high current of 8 A/g, the SA-MCO sample was able to deliver a capacity of 680 mA h/g, which is much higher than the contrast sample of MCO (375 mA h/g). The charge/discharge curves tested under different current densities of MCO and SA-MCO (Figure S9) were also examined to further reveal the performance different between the two samples. To have a better understanding on the battery performance, the EIS of these two samples after cycling were tested. The SA-MCO sample with a hierarchical structure showed a much smaller radius (26 Ω) of the

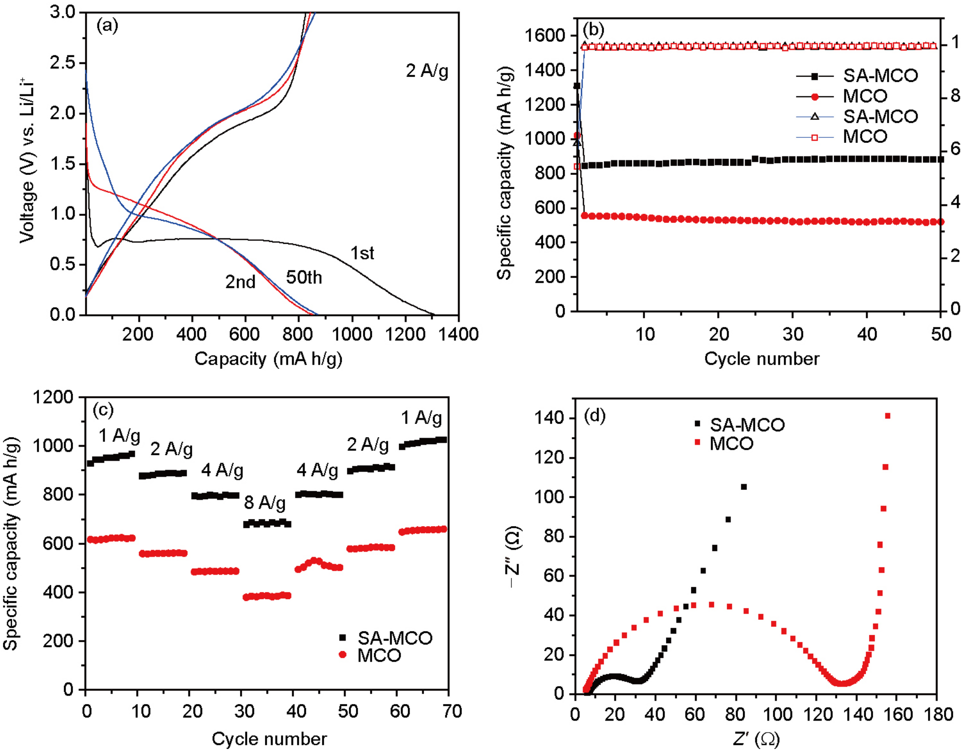

Figure 5 (a) The 1st, 2nd, and 50th charge-discharge profiles for the SA-MCO sample at a current density of 2 A/g; (b) long-term cycling performance and Columbic efficiency of the MCO and SA-MCO samples at 2 A/g; (c) rate capability test result of MCO and SA-MCO; (d) Nyquist plots of MCO and SA-MCO after 50 cycles in the frequency range from 100 kHz to 10 mHz (color online).

semicircle from the high-to-medium frequency range, revealing a much less charge transfer and surface film resistance (Rct) between electrolyte and active material as compared to the MCO sample (126 Ω). It is therefore expected that the charge-transfer interface reaction occurs more easily for a sample with more pores and higher surface area, which is able to ensure an improved electrochemical performance [12,31,32].

We reported a facile synthetic protocol for the construction of $MnCo_2O_4$ microspheres, which showed a hierarchical structure with embedded mesopores, forming favorable structural characters for high battery performance. We confirmed that sodium salicylate in our continuous-flow reaction can act as an essential additive to control the precipitation of the two involved metal cations. It can not only facilitate the formation of microspheric shape, but also act as an effective precursor for the creation of inner mesopores. We demonstrated that the hierarchically-structured $MnCo_2O_4$ showed outstanding performance when it was tested as an anode material in lithium ion batteries as revealed by its extraordinary cycling stability and high rate capability.

Acknowledgments This work was supported by the National Natural Science Foundation of China (51672282, 21373238), the National Basic Research Program of China (2013CB934000), AND the Strategic Priority Research Program of the Chinese Academy of Sciences (XDA09010101).

Conflict of interest The authors declare that they have no conflict of interest.

Supporting information The supporting information is available online at http://chem.scichina.com and http://link.springer.com/journal/11426. The supporting materials are published as submitted, without typesetting or editing. The responsibility for scientific accuracy and content remains entirely with the authors.

1 Aricò AS, Bruce P, Scrosati B, Tarascon JM, van Schalkwijk W. *Nat Mater*, 2005, 4: 366–377
2 Reddy MV, Subba Rao GV, Chowdari BVR. *Chem Rev*, 2013, 113: 5364–5457
3 Idota Y. *Science*, 1997, 276: 1395–1397
4 Choi NS, Chen Z, Freunberger SA, Ji X, Sun YK, Amine K, Yushin G, Nazar LF, Cho J, Bruce PG. *Angew Chem Int Ed*, 2012, 51: 9994–10024
5 Zeng P, Wang X, Ye M, Ma Q, Li J, Wang W, Geng B, Fang Z. *RSC Adv*, 2016, 6: 23074–23084
6 Huang G, Xu S, Xu Z, Sun H, Li L. *ACS Appl Mater Interfaces*, 2014, 6: 21325–21334
7 Wei TY, Chen CH, Chien HC, Lu SY, Hu CC. *Adv Mater*, 2010, 22: 347–351
8 Zhou L, Zhao D, Lou XW. *Adv Mater*, 2012, 24: 745–748
9 Zhou L, Wu HB, Zhu T, Lou XWD. *J Mater Chem*, 2012, 22: 827–829
10 Qiu Y, Yang S, Deng H, Jin L, Li W. *J Mater Chem*, 2010, 20: 4439–4444
11 Guo Y, Yu L, Wang CY, Lin Z, Lou XWD. *Adv Funct Mater*, 2015, 25: 5184–5189
12 Grugeon S, Laruelle S, Dupont L, Tarascon JM. *Solid State Sci*, 2003, 5: 895–904
13 Niu F, Wang N, Yue J, Chen L, Yang J, Qian Y. *Electrochim Acta*, 2016, 208: 148–155
14 Huang G, Xu S, Lu S, Li L, Sun H. *Electrochim Acta*, 2014, 135:

420–427

15 Wang L, Liu B, Ran S, Wang L, Gao L, Qu F, Chen D, Shen G. *J Mater Chem A*, 2013, 1: 2139–2143

16 Gomez J, Kalu EE. *J Power Sources*, 2013, 230: 218–224

17 Che H, Liu A, Mu J, Wu C, Zhang X. *Ceramics Int*, 2016, 42: 2416–2424

18 Lee JW, Hall AS, Kim JD, Mallouk TE. *Chem Mater*, 2012, 24: 1158–1164

19 Wang H, Cui LF, Yang Y, Sanchez Casalongue H, Robinson JT, Liang Y, Cui Y, Dai H. *J Am Chem Soc*, 2010, 132: 13978–13980

20 Li J, Xiong S, Li X, Qian Y. *Nanoscale*, 2013, 5: 2045–2054

21 Liu S, Zhang S, Xing Y, Wang S, Lin R, Wei X, He L. *Electrochim Acta*, 2014, 150: 75–82

22 Kuang M, Zhang YX, Li TT, Li KF, Zhang SM, Li G, Zhang W. *J Power Sources*, 2015, 283: 270–278

23 Li J, Wang J, Liang X, Zhang Z, Liu H, Qian Y, Xiong S. *ACS Appl Mater Interfaces*, 2014, 6: 24–30

24 Fu C, Li G, Luo D, Huang X, Zheng J, Li L. *ACS Appl Mater Interfaces*, 2014, 6: 2439–2449

25 Zhang R, Shen D, Xu M, Feng D, Li W, Zheng G, Che R, Elzatahry AA, Zhao D. *Adv Energy Mater*, 2014, 4: 1301725

26 Wang Y, Su D, Ung A, Ahn JH, Wang G. *Nanotechnology*, 2012, 23: 055402

27 Sharma Y, Sharma N, Subba Rao GV, Chowdari BVR. *Adv Funct Mater*, 2007, 17: 2855–2861

28 Chen S, Qiao SZ. *ACS Nano*, 2013, 7: 10190–10196

29 Hu L, Zhong H, Zheng X, Huang Y, Zhang P, Chen Q. *Sci Rep*, 2012, 2: 986

30 Zhang Y, Wang X, Zhao Q, Fu Y, Wang H, Shu H. *Electrochim Acta*, 2015, 180: 866–872

31 Zhang L, Hu P, Zhao X, Tian R, Zou R, Xia D. *J Mater Chem*, 2011, 21: 18279–18283

32 Li D, Zhang Y, Li L, Hu F, Yang H, Wang C, Wang Q. *Sci China Chem*, 2016, 59: 122–127